

HEART ARTIFACT REMOVAL IN ELECTROHYSTEROGRAPHY MEASUREMENTS USING ALGEBRAIC DIFFERENTIATORS

AMINE OTHMANE¹, MARIA CAMILA BUSTOS VIVAS², JOHANNES STEUER¹, JANA HUTTER³

ABSTRACT. Electrohysterography (EHG) enables non-invasive monitoring of uterine contractions but can be contaminated by electrocardiogram (ECG) artifacts. This work presents an ECG removal method using algebraic differentiators, a control-theoretic tool for model-free derivative estimation, that preserves signal shape outside the detected cardiac pulse locations. The differentiator parameters are designed to simultaneously suppress slow physiological artifacts and powerline interference while maximizing output signal-to-noise ratio. Cross-channel clustering distinguishes cardiac pulses from localized artifacts, enabling accurate pulse subtraction without auxiliary ECG references. Implemented as a causal FIR filter, the method is validated on multichannel EHG recordings from female and male subjects and compared to the template subtraction method.

1. INTRODUCTION

Electrohysterography (EHG) is a non-invasive method for recording uterine electrical activity associated with myometrial contractions [1, 2]. While EHG is increasingly used for pregnancy monitoring and preterm labor detection, recent studies furthermore highlight its relevance for analyzing uterine contractions throughout the menstrual cycle [3, 4, 5]. This muscular activity motion, referred to as uterine peristalsis, varies across cycle phases, and abnormal contractility has been linked to adenomyosis, endometriosis, and leiomyoma [1, 6]. Unlike invasive methods or imaging with limited accessibility, EHG enables non-invasive high-frequency continuous monitoring [6, 2].

However, surface recordings of electrical activities are contaminated by multiple physiological sources including electrocardiogram (ECG), electromyographic activity from abdominal muscles, and bowel movements [7, 8]. ECG artifacts pose a challenge due to the potential large amplitude of cardiac signals. Conventional ECG removal methods have significant limitations. QRS interpolation methods risk distorting the underlying neural signal dynamics [9]. Adaptive filtering requires auxiliary ECG reference channels [7]. Template subtraction assumes stationary ECG morphology and can introduce residual artifacts when the ECG waveform varies, while wavelet-based methods demand substantial computational resources or remove some low spectral components of the measured signals [10, 8]. Machine learning approaches require extensive training data and lack interpretability.

This work addresses ECG artifact removal using algebraic differentiators, a tool from control theory for model-free derivative estimation [11, 12]. Detecting sparse impulsive events (heartbeats) in signals corrupted by baseline drift and periodic interference is structurally analogous to fault detection and isolation (FDI) [13, 14]. Algebraic differentiators are well-suited for this task, providing baseline suppression and noise rejection while enabling low computational complexity through causal FIR filtering [15, 16].

The main contributions are: (i) a distributional signal model that represents impulsive physiological events, (ii) a systematic cardiac artifact removal method based on algebraic differentiators with explicit parameter design for simultaneous powerline interference suppression and baseline attenuation, including theoretical analysis of noise rejection and frequency selectivity, (iii) a cross-channel clustering algorithm exploiting spatial coherence to distinguish cardiac pulses from localized artifacts without auxiliary ECG references, and (iv) experimental validation on EHG recordings comparing the proposed method against template subtraction, demonstrating effective artifact removal that preserves signal integrity outside the detected pulse locations, with low computational complexity and no training requirements.

The remainder of the paper is organized as follows. Section 2 describes the data acquisition and formalizes the problem statement. Section 3 presents the signal decomposition model and assumptions. Section 4 details

*This work was not supported by any organization.

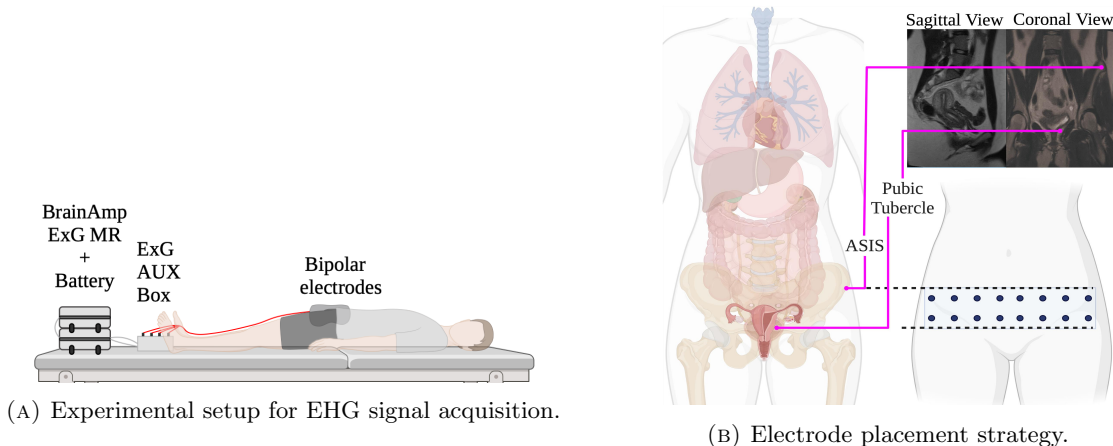


FIGURE 1. (a) EHG recording setup. (b) Electrode placement using the anterosuperior iliac spine (ASIS) and pubic bone as anatomical landmarks, shown on sagittal and coronal MRI scans.

the algebraic differentiator-based artifact removal method, including parameter design and pulse detection. Section 5 presents experimental results on EHG recordings. Finally, Section 6 concludes with a summary and outlook.

2. DATA ACQUISITION & PROBLEM STATEMENT

2.1. Data acquisition. The study population comprised two healthy volunteers, one non-pregnant woman (aged 21–30 years) and one healthy male subject (aged 24–30 years) to identify uterine-specific signal components absent in male recordings. Participants lay supine with minimal movement (Figure 1a), skin preparation was performed with abrasive gel reduced electrode impedance below 10Ω . Electrodes were placed between the anterosuperior iliac spine (ASIS) and pubic bone, with a ground electrode on one hip (Figure 1b). EHG signals were recorded using a multichannel BrainAmp ExG MR amplifier (Brain Products, Gilching, Germany) with eight bipolar electrodes at a sampling frequency of $f_s = 5\text{ kHz}$ for at least seven minutes per subject.

2.2. Problem statement. The goal is to extract uterine-specific signal components from multichannel EHG recordings contaminated by ECG artifacts. Formally, given an observed signal $x_i(t)$ in channel i , we seek to estimate the artifact-free signal by detecting and removing cardiac pulse contributions while preserving uterine activity, baseline physiological components, and minimizing signal distortion. The method should operate without auxiliary ECG reference channels and be suitable for real-time processing.

3. MATHEMATICAL MODEL

Abdominal surface electromyography captures the superimposed electrical activity of multiple physiological sources. We consider an m -channel EHG signal $\mathbf{x}(t) = [x_1(t), \dots, x_m(t)]^T \in \mathbb{R}^m$ observed over $t \in [0, T_{\text{obs}}]$ and sampled at frequency f_s .

3.1. Signal Model. Each physiological source can generate discrete events (e.g., heartbeats, uterine contractions, bowel contractions) that propagate through the abdominal tissue via volume conduction and are detected as EHG signals. The primary objective is to decompose the observed multi-channel signal into a cardiac component consisting of impulse trains from heartbeats, a uterine component, a bowel component, and a residual baseline containing respiratory artifacts and other unmodeled sources.

The observed EHG signal in each channel $i \in \{1, \dots, m\}$ is modeled as a superposition of physiological impulse trains from multiple organs, an unknown baseline signal, and deterministic power supply interference.

In the distributional sense, we have

$$x_i(t) = \nu_i(t) + \sum_{\ell \in \mathcal{L}} \sum_{j=1}^{N_\ell} a_\ell^{(j)} \delta(t - t_\ell^{(j)} - \tau_{i,\ell}) + h_i(t) + \eta_i(t), \quad (1)$$

where $\nu_i : [0, T_{\text{obs}}] \rightarrow \mathbb{R}$ represents slow-varying components satisfying Assumption 1, $\mathcal{L} = \{\text{Heart, Bowel, Uterus, Bladder}\}$ is the set of physiological sources, $N_\ell \in \mathbb{N}_0$ is the number of events from source ℓ during the observation period, $a_\ell^{(j)} \in \mathbb{R}$ is the amplitude of the j -th impulse from source ℓ , δ denotes the Dirac delta distribution, $t_\ell^{(j)} \in (0, T_{\text{obs}})$ is the occurrence time of the j -th event at source ℓ , $\tau_{i,\ell} \geq 0$ is the propagation delay from source ℓ to channel i (accounting for finite signal propagation velocity through tissue and spatial sensor distribution), $h_i : [0, T_{\text{obs}}] \rightarrow \mathbb{R}$ represents the power supply interference, and η_i represents additive measurement noise with $\mathbb{E}[\eta_i(t)] = 0$.

The power supply interference h_i is modeled as $h_i(t) = \sum_{q=1}^Q A_{i,q} \sin(2\pi q f_0 t + \phi_{i,q})$, where $f_0 = 50$ Hz is the fundamental power line frequency, $Q \in \mathbb{N}$ is the number of harmonics, $A_{i,q} \geq 0$ are the harmonic amplitudes, and $\phi_{i,q} \in [0, 2\pi)$ are the channel-dependent phase offsets.

3.2. Model Assumptions and Discussion. The model (1) relies on two key idealizations: the Dirac delta representation of impulsive events and the smoothness of the baseline signal. Both are motivated by temporal scale separation inherent in EHG signals. Physiologically, impulsive events such as cardiac R-waves (10–20 ms), uterine electromyographic bursts (100–500 ms), and bowel peristaltic events (seconds to tens of seconds, often occurring as propagating spike-burst complexes) create sharp transients [17, 8]. In contrast, baseline components arising from respiratory modulation (0.2–0.5 Hz) and postural drift (minutes) vary on much longer time scales [7]. Since pulse durations are much shorter than baseline variation scales ($\tau_{\text{baseline}} \sim 2\text{--}5$ s), impulsive events appear instantaneous relative to baseline dynamics, justifying the Dirac representation.

Assumption 1 (Locally smooth baseline). For each channel $i \in \{1, \dots, m\}$, the baseline signal $\nu_i \in C^n([0, T_{\text{obs}}])$ is at least n times continuously differentiable, where $n \in \mathbb{N}$ is the derivative order. Moreover, there exists $\epsilon > 0$ such that $\sup_{t \in [0, T_{\text{obs}}]} |\nu_i^{(n)}(t)| < \epsilon$, where ϵ is small relative to the peak magnitudes of the n -th derivatives of the impulsive components. This enables separation of impulsive events from the slowly-varying baseline via higher-order differentiation: ν_i can be locally approximated by polynomials of degree less than n with error $\mathcal{O}(T_w^{n+1})$ within each analysis window of length T_w .

The derivative order n should be chosen sufficiently large to attenuate respiratory and postural components while remaining below the order at which numerical differentiation becomes dominated by measurement noise. The following section develops an artifact removal algorithm that exploits this model structure.

4. ARTIFACT REMOVAL VIA PULSE DETECTION AND RECONSTRUCTION

This section presents a systematic approach to cardiac artifact removal that exploits the impulsive nature of cardiac pulses. Algebraic differentiation with carefully chosen parameters transforms the signal model (1) into a form where impulsive components dominate over baseline drift, power line interference, and measurement noise. Threshold-based detection identifies pulse start times in each channel, and cross-channel clustering distinguishes cardiac pulses from localized artifacts. Amplitude estimation and signal reconstruction then subtract only cardiac pulses, preserving EHG activity.

4.1. Pulse Indicator Design. To enhance impulse detection, we compute the n -th order derivative of the signal x_i in channel $i \in \{1, \dots, m\}$ using algebraic differentiation (see, e.g., [11] for original derivations and [12] for a survey on parametrization, interpretations, and numerous applications). The n -th order time derivative of x_i is then approximated by $\hat{x}_i^{(n)}(t)$ defined as

$$\hat{x}_i^{(n)}(t) = \int_{t-T}^t g^{(n)}(t-\tau) x_i(\tau) d\tau, \quad (2)$$

where $g^{(n)}$ is the n -th order derivative of a causal kernel g with compact support $[0, T]$ (with T in seconds). The kernel is constructed from weighted Jacobi polynomials $P_j^{(\alpha, \beta)}(\nu)$ for $j = 0, 1, \dots, N$, which form an

orthogonal basis with respect to the weight function

$$w(\nu) = \begin{cases} (1-\nu)^\alpha(1+\nu)^\beta, & \nu \in [-1, 1], \\ 0, & \text{otherwise,} \end{cases}$$

for $\alpha, \beta > -1$. The affine transformation $\nu(\tau) = 1 - 2\tau/T$ maps $[0, T]$ to $[-1, 1]$. Truncating the polynomial expansion at order $N \in \mathbb{N}_0$ yields

$$g(\tau) = \frac{2}{T} w(\nu(\tau)) \sum_{j=0}^N \frac{P_j^{(\alpha, \beta)}(\vartheta)}{\|P_j^{(\alpha, \beta)}\|_{L_w^2}^2} P_j^{(\alpha, \beta)}(\nu(\tau)),$$

where $\vartheta \in [-1, 1]$ is a delay parameter and $\|P_j^{(\alpha, \beta)}\|_{L_w^2}^2 := \int_{-1}^1 |P_j^{(\alpha, \beta)}(\nu)|^2 w(\nu) d\nu$ is the weighted L^2 -norm. Higher-order derivative kernels $g^{(n)}$ are obtained by successive differentiation. This operator acts as a causal low-pass filter.

Applying the differentiation operation (2) to the signal model (1), the derivative signal becomes

$$\hat{x}_i^{(n)}(t) = \hat{x}_{i, \text{pulse}}^{(n)}(t) + \hat{v}_i^{(n)}(t) + \hat{h}_i^{(n)}(t) + \hat{\eta}_i^{(n)}(t), \quad (3)$$

where $\hat{x}_{i, \text{pulse}}^{(n)}(t) = \sum_{\ell, j} a_\ell^{(j)} g^{(n)}(t - t_{i, \ell}^{(j)})$, $t_{i, \ell}^{(j)} = t_\ell^{(j)} + \tau_{i, \ell}$ denotes the arrival time of the j -th pulse from source ℓ at channel i , and $\hat{v}_i^{(n)}$, $\hat{h}_i^{(n)}$, $\hat{\eta}_i^{(n)}$ are the n -th derivatives of the baseline, power supply interference, and noise, respectively. By the translation property of convolution, each impulse $\delta(t - t_{i, \ell}^{(j)})$ is transformed into the shifted kernel $g^{(n)}(t - t_{i, \ell}^{(j)})$, providing a characteristic signature for detection.

With suitable parametrization of g (i.e., appropriate choice of α , β , N , ϑ , and T), the shifted kernels $g^{(n)}(t - t_{i, \ell}^{(j)})$ dominate the derivative signal $\hat{x}_i^{(n)}(t)$ compared to $\hat{v}_i^{(n)}(t)$, $\hat{h}_i^{(n)}(t)$, and $\hat{\eta}_i^{(n)}(t)$, enabling $\hat{x}_i^{(n)}$ to serve as an effective pulse indicator. The parametrization exploits frequency-domain properties to attenuate power supply interference and the low-pass characteristics to suppress baseline components, as formalized below.

4.2. Parametrizations for Artifact Suppression. For $N = 0$ and symmetric parameters $\alpha = \beta$, the Fourier transform of g admits infinitely many zeros corresponding to the zeros of the Bessel function J_ν of the first kind of order $\nu = \alpha + 1/2$.

Power interference suppression. Let $j_{\nu, k} > 0$ denote the k -th positive zero of J_ν . For line frequency $f_0 = 50$ Hz, set $\omega_0 = 2\pi f_0$ and choose

$$T = 2j_{\alpha+1/2, k} / \omega_0. \quad (4)$$

This yields $\mathcal{G}(\omega_0) = 0$, annihilating the fundamental harmonic. Since $|\mathcal{G}(\omega)| = \mathcal{O}(|\omega|^{-(\alpha+1)})$ [16] and differentiation introduces $|\omega|^n$, the power interference at harmonics $\omega_q = q\omega_0$ satisfies $|\mathcal{F}\{\hat{h}_i^{(n)}\}(\omega_q)| = \mathcal{O}(q^{n-\alpha-1})$, for $q \rightarrow \infty$. Choosing $\alpha > n - 1$ ensures asymptotic decay for all harmonics $q \geq 2$.

Noise amplification analysis. Assume η_i is a zero-mean wide-sense stationary process with power spectral density S_{η_i} . The convolution (2) transforms the power spectral density as $S_{\hat{\eta}_i^{(n)}}(\omega) = |\omega|^{2n} |\mathcal{G}(\omega)|^2 S_{\eta_i}(\omega)$. For white noise with $S_{\eta_i}(\omega) = S_0$, the variance satisfies

$$\sigma_n^2 := \text{Var}[\hat{\eta}_i^{(n)}(t)] = \frac{S_0}{2\pi} \int_{-\infty}^{\infty} |\omega|^{2n} |\mathcal{G}(\omega)|^2 d\omega.$$

Since the kernel g has compact support $[0, T]$, this integral is always finite. However, since $|\mathcal{G}(\omega)|^2 = \mathcal{O}(|\omega|^{-2(\alpha+1)})$, the noise amplification scales as $\mathcal{O}(|\omega|^{2n-2(\alpha+1)})$ at high frequencies. Larger values of α relative to n reduce noise amplification by accelerating the asymptotic decay of the kernel's frequency response. For an in-depth analysis of noise amplification in algebraic differentiators, see e.g., [16, 18], and [12].

Detectability condition. Define $A_{\text{peak}} := \min_{\ell, j} |a_\ell^{(j)}| \cdot \|g^{(n)}\|_\infty$ as the minimum peak impulsive magnitude. By Assumption 1 with $\|\hat{v}_i^{(n)}\|_\infty < \epsilon$, and the preceding analysis, $\hat{x}_i^{(n)}$ serves as an effective pulse indicator when

$$\max\{\epsilon, \|\hat{h}_i^{(n)}\|_\infty, \|\hat{\eta}_i^{(n)}\|_\infty\} \ll A_{\text{peak}}. \quad (5)$$

4.3. Threshold-Based Pulse Start Time Detection. The derivative signal (3) decomposes as

$$\hat{x}_i^{(n)}(t) = \hat{x}_{i,\text{pulse}}^{(n)}(t) + \hat{x}_{i,\text{artifact}}^{(n)}(t),$$

where $\hat{x}_{i,\text{artifact}}^{(n)} := \hat{v}_i^{(n)} + \hat{h}_i^{(n)} + \hat{\eta}_i^{(n)}$ combines all artifact components. Under the detectability condition (5), peaks in $|\hat{x}_i^{(n)}(t)|$ are dominated by impulsive components.

For each channel $i \in \{1, \dots, m\}$ and derivative order $n \in \mathbb{N}$, let $\{|\hat{x}_i^{(n)}[k]| : k = 1, \dots, K\}$, where $x[k] := x(k/f_s)$ denotes the sampled signal, be the magnitude sequence over the observation window. Define $\tau_p^{(i)}$ as the p -th percentile of this empirical distribution. Candidate impulse times are identified at sample indices k satisfying $|\hat{x}_i^{(n)}[k]| > \tau_p^{(i)}$. Let $\mathcal{T}_i^{(n)} = \{k_1^{(i)}, \dots, k_{M_i}^{(i)}\}$ with $k_1^{(i)} < \dots < k_{M_i}^{(i)}$ denote these ordered threshold crossings. Under scale separation (5) and pulse sparsity, the percentile p should satisfy $p > 100(1 - N_{\text{beats}} \cdot Tf_s/K)$, where N_{beats} is the expected number of heartbeats and K is the total number of samples, ensuring the threshold lies above artifact levels but below pulse magnitudes.

To avoid multiple detections from a single impulse, crossings within $L_{\min} = \lceil Tf_s \rceil$ samples are consolidated. The filtered detection set $\mathcal{D}_i^{(n)} \subseteq \mathcal{T}_i^{(n)}$ is constructed iteratively: initialize $\mathcal{D}_i^{(n)} = \{k_1^{(i)}\}$, then for $j = 2, \dots, M_i$, add $k_j^{(i)}$ to $\mathcal{D}_i^{(n)}$ if and only if $k_j^{(i)} - \max \mathcal{D}_i^{(n)} \geq L_{\min}$. This consolidation exploits the compact support $[0, T]$ of $g^{(n)}$: a single impulse cannot generate threshold crossings separated by more than $\lceil Tf_s \rceil$ samples.

For each detection $k_j^{(i)} \in \mathcal{D}_i^{(n)}$, we estimate the pulse start time at channel i from the first zero-crossing $z_j^{(i)}$ of $\hat{x}_i^{(n)}$ following the peak magnitude at $k_j^{(i)}$, which is more robust to noise than preceding zero-crossings.

4.4. Cross-Channel Cardiac Pulse Clustering. Cardiac events propagate across all channels with small inter-channel delays, while localized artifacts (bowel movements, motion) affect fewer channels. This spatial coherence enables unsupervised cardiac pulse identification by clustering detections from all channels $i = 1, \dots, m$.

Collect all detected pulses into $\mathcal{P} = \{(t_j^{(i)}, i, j) : i \in \{1, \dots, m\}, j \in \mathcal{D}_i^{(n)}\}$ and sort by time. Group pulses into candidate beat groups \mathcal{B}_m ($m = 1, 2, \dots$) using temporal window $\Delta t_{\text{beat}} \in [20, 50]$ ms: initialize \mathcal{B}_1 with the earliest pulse, then for each subsequent pulse $(t, i, j) \in \mathcal{P}$, add it to the current group \mathcal{B}_m if $t - \max\{t' : (t', \cdot, \cdot) \in \mathcal{B}_m\} \leq \Delta t_{\text{beat}}$, otherwise start a new group \mathcal{B}_{m+1} . Classify \mathcal{B}_m as cardiac if $N_{\text{ch}}(\mathcal{B}_m) = |\{i : (\cdot, i, \cdot) \in \mathcal{B}_m\}| \geq \lceil \rho \cdot m \rceil$ with $\rho \in [0.5, 0.7]$; otherwise mark as artifact. Within each cardiac beat group \mathcal{B}_m , compute median time $\bar{t}_m = \text{median}\{t : (t, \cdot, \cdot) \in \mathcal{B}_m\}$ and retain per channel only the detection $(t_j^{(i)}, i, j)$ minimizing $|t_j^{(i)} - \bar{t}_m|$. Parameters Δt_{beat} and ρ are determined empirically, balancing sensitivity and false positives.

Remark 1 (Algorithm limitations). The greedy grouping may merge nearby beats when inter-beat intervals approach $2\Delta t_{\text{beat}}$, and the hard channel participation threshold lacks adaptivity to varying SNR conditions. These limitations could be addressed through adaptive clustering algorithms and dynamic threshold adjustment based on signal quality metrics.

4.5. Amplitude Estimation and Signal Reconstruction. Following cardiac pulse clustering, let $\mathcal{C}_i \subseteq \mathcal{D}_i^{(n)}$ denote the subset of detections classified as cardiac pulses in channel i , with $|\mathcal{C}_i| = N_i$ cardiac pulses. For the m -th cardiac detection ($m = 1, \dots, N_i$) with zero-crossing $z_m^{(i)}$, define $t_m := z_m^{(i)} f_s^{-1}$ and the time-shifted kernel $g_{\delta_m}^{(n)}(t) = g^{(n)}(t - t_m + t_0)$, where t_0 is the zero-crossing of $g^{(n)}(t)$. The amplitude $\hat{a}_m^{(i)}$ is estimated via least squares over $\mathcal{W}_m = [t_m, t_m + T]$, yielding

$$\hat{a}_m^{(i)} = \frac{\sum_{k \in \mathcal{I}_m} \hat{x}_i^{(n)}[k] g_{\delta_m}^{(n)}[k]}{\sum_{k \in \mathcal{I}_m} \left(g_{\delta_m}^{(n)}[k]\right)^2},$$

where \mathcal{I}_m denotes sample indices in \mathcal{W}_m . The artifact-free signal

$$x_{i,\text{clean}}(t) = \int_{t-T}^t g(t-\tau) x_i(\tau) d\tau - \hat{x}_{i,\text{pulse}}^{(0)}(t),$$

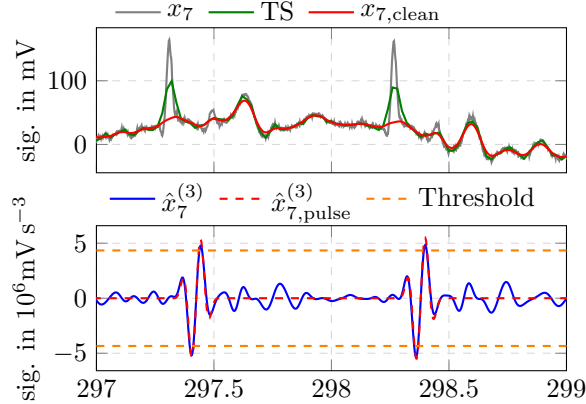


FIGURE 2. Artifact removal for channel seven (male subject). Top: raw signal (gray), proposed method (red), and template subtraction (green). Bottom: derivative signal with detected pulses and threshold.

is obtained by subtracting only the reconstructed cardiac pulse component from the filtered signal, where $g_{\delta_m}^{(0)}(t) = g(t - t_m + t_0)$ and the cardiac pulse component is reconstructed as

$$\hat{x}_{i, \text{pulse}}^{(0)} = \sum_{m=1}^{N_i} \hat{a}_m^{(i)} g_{\delta_m}^{(0)}(t).$$

This removes cardiac artifacts, power line interference, baseline drift, and high-frequency noise while preserving EHG activity.

4.6. Optimal Differentiator Parameters. The preceding analysis constrains $\alpha > n - 1$ and determines T via (4), where $k \in \mathbb{N}$ indexes the k -th positive zero of $J_{\alpha+1/2}$. The remaining parameters (n, α, k) are selected offline on representative data to maximize the output SNR defined as

$$\text{SNR}_{\text{out}} := \frac{\|\hat{x}_{i, \text{pulse}}^{(n)}\|_{L^2}^2}{\|\hat{x}_i^{(n)} - \hat{x}_{i, \text{pulse}}^{(n)}\|_{L^2}^2}. \quad (6)$$

This optimization balances noise amplification (increasing with n , decreasing with α), window length (determined by k), and pulse signature enhancement ($\|g^{(n)}\|_{\infty}$), and can be performed numerically over a discrete grid. The following section uses parameters computed using this approach.

5. EXPERIMENTAL RESULTS

Approximating (2) with the mid-point rule yields a causal FIR filter of length $L = \lceil T f_s \rceil$ samples [12]. The results use parameters $n = 3$, $\alpha = 12$, and $k = 6$ (6th Bessel zero), yielding from (4) the window length $T \approx 112.9$ ms and $L = 565$ at $f_s = 5$ kHz.

Figures 2 and 3 show representative results for two channels from the male subject. The top panels display the raw signal x_i (gray) and the cleaned signal $x_{i, \text{clean}}$ from the proposed method (red) and template subtraction (green) from [8] (the toolbox from [19] has been used for the data processing). The bottom panels show the derivative signal $\hat{x}_i^{(3)}$ with detected pulse signatures and the percentile-based threshold. The inter-peak intervals of approximately 1 s correspond to a heart rate of 60 bpm, confirming that the detected pulses are cardiac artifacts. The proposed method effectively removes these artifacts while preserving the underlying signal structure. The SNR_{out} defined in (6) for these two examples are 5.14 dB and 7.42 dB, respectively.

Figure 4 shows results for an electrode near the uterus in the female subject. The derivative exhibits visible distortions because uterine activity violates $\hat{x}_{i, \text{base}}^{(n)}(t) \approx 0$. Slow-varying uterine components produce non-zero derivatives erroneously attributed to cardiac artifacts, limiting effectiveness for electrodes in close uterine proximity. The SNR_{out} for this example is -2.15 dB.

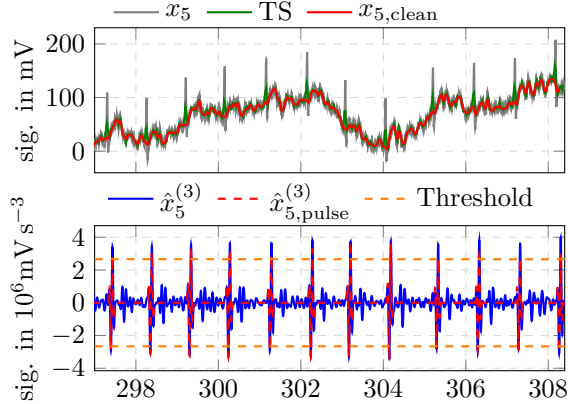


FIGURE 3. Artifact removal for channel five (male subject). Top: raw signal (gray), proposed method (red), and template subtraction (green). Bottom: derivative signal with detected pulses and threshold.

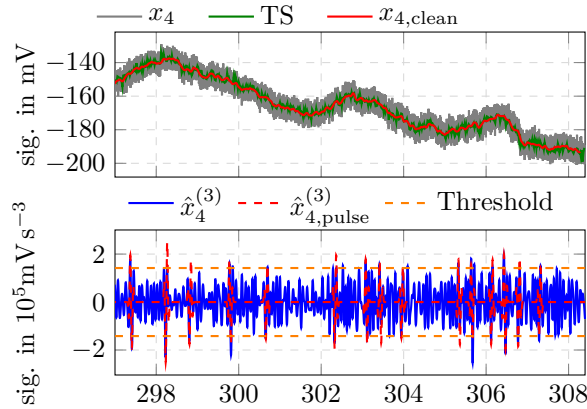


FIGURE 4. Artifact removal for channel four (female subject, electrodes close to uterus). Top: raw signal (gray), proposed method (red), and template subtraction (green). Bottom: derivative signal with detected pulses and threshold.

Figure 5 shows inter-channel delays estimated from detected cardiac pulse times relative to channel 8. Negative delays indicate earlier wavefront arrival, positive delays later arrival. Median delays range from -11.6 ms (channel 7) to 3.0 ms (channel 2), reflecting spatial propagation of cardiac electrical activity across the electrode array. The total delay spread of approximately 15 ms corresponds to an apparent conduction velocity of $3\text{--}7$ m s^{-1} for typical electrode spacings of $5\text{--}10$ cm, consistent with volume-conducted cardiac signals. The tight interquartile ranges (1 ms to 2 ms) confirm consistent detection and validate the spatial coherence assumption.

6. CONCLUSION AND OUTLOOK

An algebraic differentiator-based approach for removing maternal cardiac artifacts from EHG signals has been presented. Differentiation enhances impulsive cardiac signatures, enabling detection via percentile thresholding and artifact reconstruction. Experimental results demonstrate effective removal without an ECG reference, with consistent inter-channel delays validating the spatial coherence assumption.

The current approach assumes $\hat{x}_{i,\text{base}}^{(n)}(t) \approx 0$. While this holds for electrodes distant from the uterus, electrodes near uterine tissue may capture slow-varying components that violate this assumption. Future work should extend the signal model to accommodate non-zero baseline derivatives, e.g., using methods from system identification. The estimated inter-channel propagation delays are a key byproduct of the method

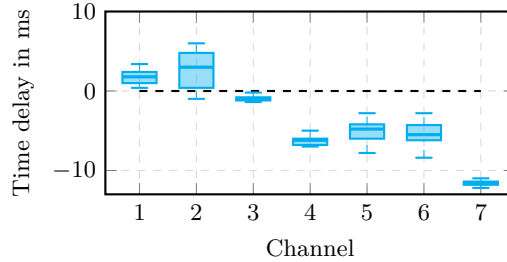


FIGURE 5. Inter-channel delays of detected cardiac pulses relative to channel 8.

and warrant further investigation, as they may provide insights into cardiac signal propagation patterns or electrode placement quality. Additional directions include parameter sensitivity analysis, quantitative benchmarking, and validation across a larger patient cohort.

REFERENCES

- [1] N. P. M. Kuijsters, W. G. Methorst, M. S. Q. Kortenhorst, C. Rabotti, M. Mischi, and B. C. Schoot, "Uterine peristalsis and fertility: current knowledge and future perspectives: a review and meta-analysis," *Reprod. Biomed. Online*, vol. 35, no. 1, pp. 50–71, 2017.
- [2] R. E. Garfield and W. L. Maner, "Physiology and electrical activity of uterine contractions," *Semin. Cell Dev. Biol.*, vol. 18, no. 3, pp. 289–95, 2007.
- [3] J. Alberola-Rubio, J. M. Mira-Tomas, A. Diaz-Martinez, P. Alama Faubel, S. Caballero Sanz, G. Castellón Cortés, M. de Arriba-Garcia, J. Llácer, and J. Garcia-Casado, "Objective and comprehensive characterization of uterine peristaltic activity throughout the menstrual cycle by means of intracavitary electrohysterography, a cohort study," *Acta Obstet. Gynecol. Scand.*, vol. 105, no. 1, pp. 156–165, 2026.
- [4] C. Rabotti, F. Sammal, N. Kuijsters, B. Schoot, M. Kortenhorst, and M. Mischi, "Analysis of uterine activity in non-pregnant women by electrohysterography: A feasibility study," in *2015 37th Annual International Conference of the IEEE Engineering in Medicine and Biology Society (EMBC)*, pp. 5916–5919.
- [5] S. Wang, K. Anderson, S. Pizzella, H. Xu, W. Wang, Z. Wen, Y. Nan, J. Lau, Q. Wang, V. Ratts, and Y. Wang, "Noninvasive imaging of 4d electrical activation patterns of uterine peristalsis during normal menstrual cycles," *npj Women's Health*, vol. 2, no. 1, 2024.
- [6] M. J. Harmsen, L. M. Trommelen, R. A. de Leeuw, T. Tellum, L. J. M. Juffermans, A. W. Griffioen, I. Thomassin-Naggara, T. Van den Bosch, and J. A. F. Huirne, "Uterine junctional zone and adenomyosis: comparison of mri, transvaginal ultrasound and histology," *Ultrasound Obstet. Gynecol.*, vol. 62, no. 1, pp. 42–60, 2023.
- [7] S. Abbaspour and A. Fallah, "Removing ECG artifact from the surface EMG signal using adaptive subtraction technique," *J. Biomed. Phys. Eng.*, vol. 4, no. 1, p. 33, 2014.
- [8] E. Petersen, J. Sauer, J. Graßhoff, and P. Rostalski, "Removing cardiac artifacts from single-channel respiratory electromyograms," *IEEE Access*, vol. 8, pp. 30 905–30 917, 2020.
- [9] M. J. Stam, B. C. M. van Wijk, P. Sharma, M. Beudel, D. A. Piña-Fuentes, R. M. A. de Bie, P. R. Schuurman, W.-J. Neumann, and A. W. G. Buijink, "A comparison of methods to suppress electrocardiographic artifacts in local field potential recordings," *Clin. Neurophysiol.*, vol. 146, pp. 147–161, 2023.
- [10] N. Miljković, N. Popović, O. Djordjević, L. Konstantinović, and T. B. Šekara, "Ecg artifact cancellation in surface emg signals by fractional order calculus application," *Comput. Methods Programs Biomed.*, vol. 140, pp. 259–264, 2017.
- [11] M. Mboup, C. Join, and M. Fliess, "Numerical differentiation with annihilators in noisy environment," *Numer. Algor.*, vol. 50, no. 4, pp. 439–467, 2009.
- [12] A. Othmane, L. Kiltz, and J. Rudolph, "Survey on algebraic numerical differentiation: historical developments, parametrization, examples, and applications," *Int. J. Syst. Sci.*, vol. 53, no. 9, pp. 1848–1887, 2022.
- [13] P. M. Frank, "Fault diagnosis in dynamic systems using analytical and knowledge-based redundancy: A survey and some new results," *Automatica*, vol. 26, no. 3, pp. 459–474, 1990.
- [14] Z. Gao, C. Cecati, and S. X. Ding, "A survey of fault diagnosis and fault-tolerant techniques—part I: Fault diagnosis with model-based and signal-based approaches," *IEEE Trans. Ind. Electron.*, vol. 62, no. 6, pp. 3757–3767, 2015.
- [15] L. Kiltz, C. Join, M. Mboup, and J. Rudolph, "Fault-tolerant control based on algebraic derivative estimation applied on a magnetically supported plate," *Control Eng. Pract.*, vol. 26, pp. 107–115, 2014.
- [16] L. Kiltz and J. Rudolph, "Parametrization of algebraic numerical differentiators to achieve desired filter characteristics," in *Proc. of the 52nd IEEE Conf. on Decision and Control*, Florence, Italy, 2013, pp. 7010–7015.
- [17] R. W. van Leuteren, G. J. Hutten, C. G. de Waal, P. Dixon, A. H. van Kaam, and F. H. de Jongh, "Processing transcutaneous electromyography measurements of respiratory muscles, a review of analysis techniques," *J. Electromyogr. Kinesiol.*, vol. 48, pp. 176–186, 2019.
- [18] M. Mboup and S. Riachy, "Frequency-domain analysis and tuning of the algebraic differentiators," *Int. J. Control*, vol. 91, no. 9, pp. 2073–2081, 2018.

[19] A. Delorme and S. Makeig, "EEGLAB: an open source toolbox for analysis of single-trial EEG dynamics including independent component analysis," *Journal of Neuroscience Methods*, vol. 134, no. 1, pp. 9–21, 2004.

¹AMINE OTHMANE AND JOHANNES STEUER ARE WITH SYSTEMS MODELING AND SIMULATION, SAARLAND UNIVERSITY, GERMANY AMINE.OTHMANE@UNI-SAARLAND.DE

²MARIA CAMILA BUSTOS VIVAS IS WITH THE RADIOLOGY DEPARTMENT, UNIKLINIKUM ERLANGEN, GERMANY MARIA.V.BUSTOS@FAU.DE

³JANA HUTTER IS WITH THE INSTITUTE FOR INFORMATION PROCESSING, UNIVERSITY OF HANOVER, GERMANY HUTTER@TNT.UNI-HANNOVER.DE